Supplemental Fig. 1

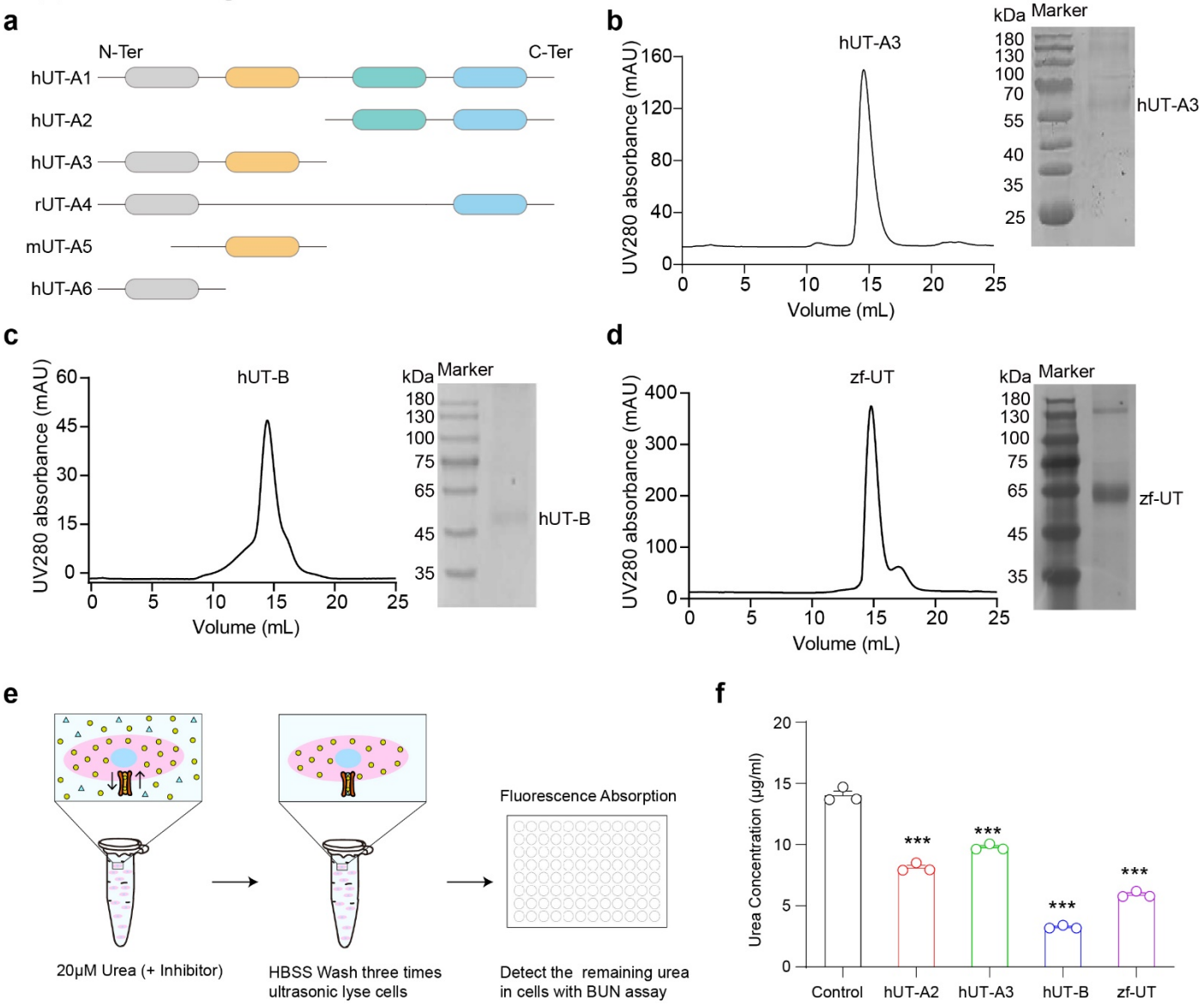

Supplementary Fig. 1 The biochemical characterization of hUT-A2, hUT-A3, hUT-B and zf-UT.

a. Schematic representation of the protein sequence of different isoforms of UT-A urea transporters.

b-d. The size-exclusion chromatography elution profiles of the purified hUT-A3 (b), hUT-B (c) and zf-UT (d). The Coomassie brilliant blue staining of corresponding protein without cross-link by glutaraldehyde were shown on the right. The elution volume of size-exclusion chromatography peak of these UTs were all at approximately 14.5 ml, indicating a homotrimer states.

e. Schematic diagram of the detection of urea transportation by UT using the urease assay kit

f. urea permeability shown by the detection of remaining urea left in cells. Data are represented as mean ± SEM from 3 independent experiments (n = 3). ***P < 0.001 by the unpaired Student's t-test (compared with control).

Supplemental Fig. 2

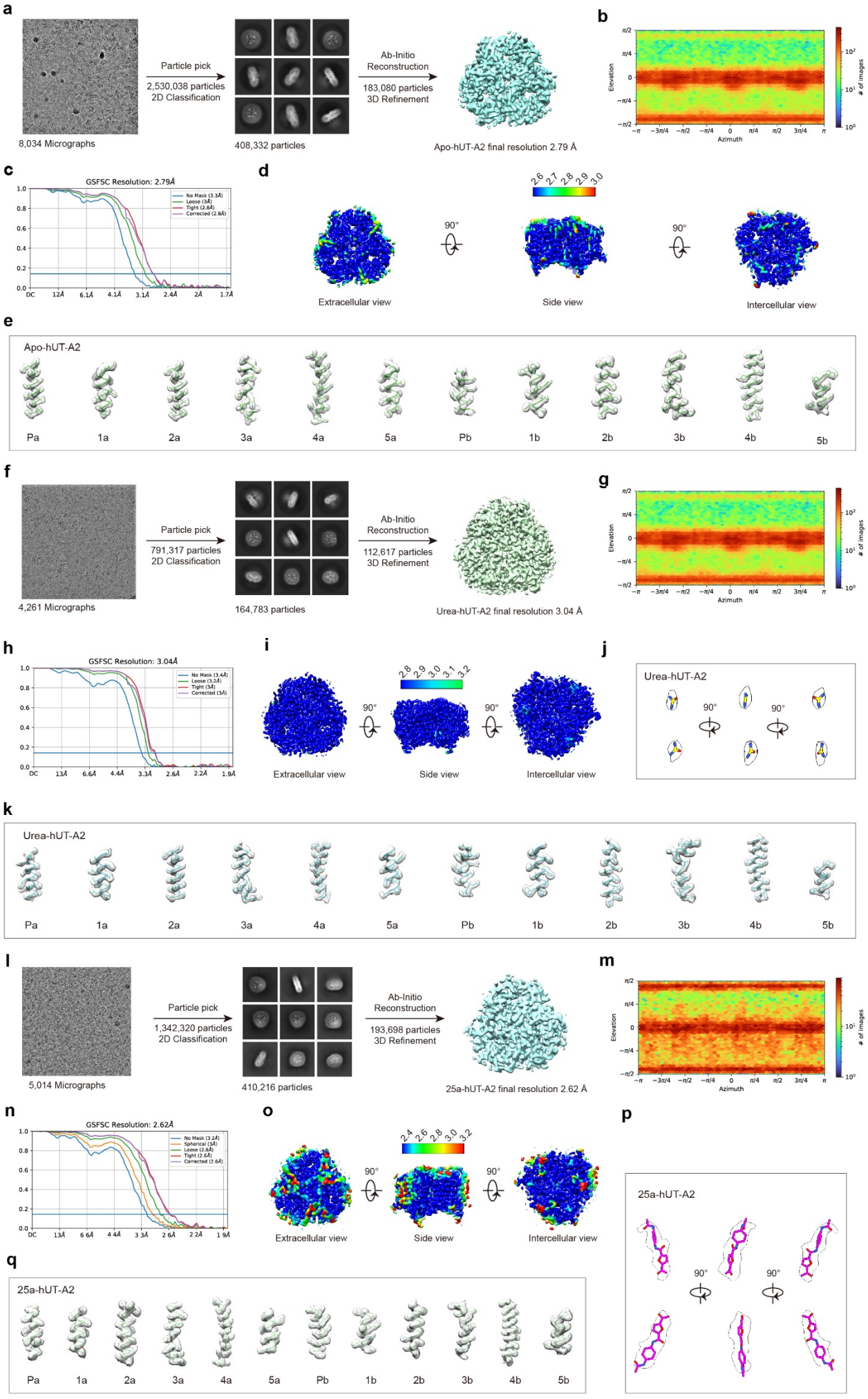

Supplementary Fig. 2 Calculation processes of the apo/urea/25a-hUT-A2.

a-e. Calculation processes of the apo-hUT-A2 structure using the cryoSPARC. Representative cryo-EM micrograph, 2D class averages and the refined map of apo -hUT-A2 structure were shown (a) with the orientation distribution histogram figures (b) and the Fourier shell correlation curves (c) for the final 3D density map which was further colored according to local resolution (Å) (d). The cryo-EM density maps and models were shown for main helices of apo-hUT-A2 structure (e).

f-k. Calculation processes of the urea-hUT-A2 structure using the cryoSPARC. Representative cryo-EM micrograph, 2D class averages and the refined map of urea-hUT-A2 structure were shown (f) with the orientation distribution histogram figures (g) and the Fourier shell correlation curves (h) for the final 3D density map which was further colored according to local resolution (Å) (i). The cryo-EM density maps and models were shown for the urea (j) and the main helices of urea-hUT-A2 structure (k).

l-q. Calculation processes of the 25a-hUT-A2 structure using the cryoSPARC. Representative cryo-EM micrograph, 2D class averages and the refined map of 25a-hUT-A2 structure were shown (l) with the orientation distribution histogram figures (m) and the Fourier shell correlation curves (n) for the final 3D density map which was further colored according to local resolution (Å) (o). The cryo-EM density maps and models were shown for the 25a (p) and the main helices of apo-zf-UT structure (q).

Supplemental Fig. 3

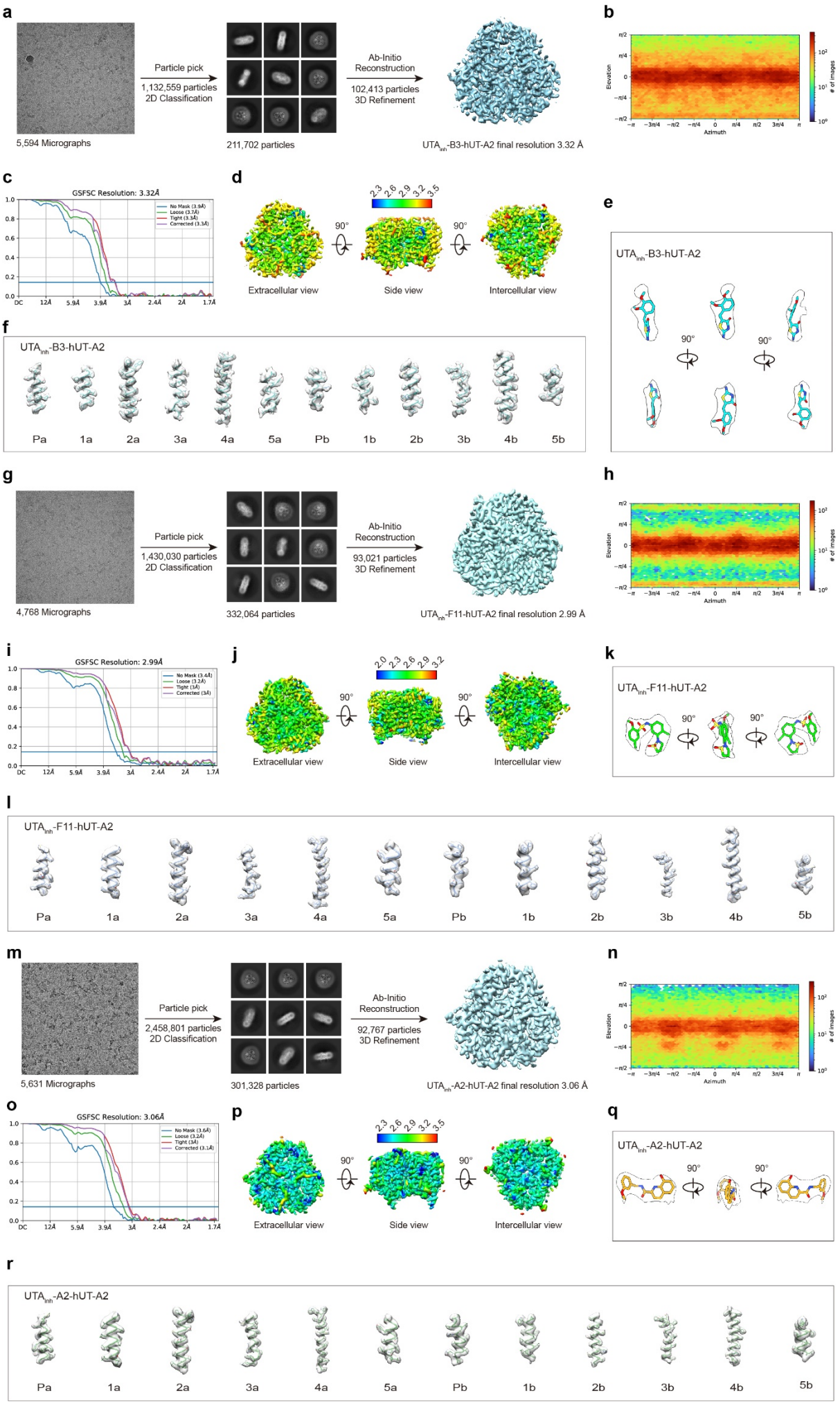

Supplementary Fig. 3 Calculation processes of the UTA_{inh}-B3/F11/A2-hUT-A2 structures.

a-f. Calculation processes of the UTA_{inh}-B3-hUT-A2 structure using the cryoSPARC. Representative cryo-EM micrograph, 2D class averages and the refined map of UTA_{inh}-B3-hUT-A2 structure were shown (a) with the orientation distribution histogram figures (b) and the Fourier shell correlation curves (c) for the final 3D density map which was further colored according to local resolution (Å) (d). The cryo-EM density maps and models were shown for UTA_{inh}-B3 (e) and the main helices of UTA_{inh}-B3-hUT-A2 structure (f).

g-l. Calculation processes of the UTA_{inh}-F11-hUT-A2 structure using the cryoSPARC. Representative cryo-EM micrograph, 2D class averages and the refined map of UTA_{inh}-F11-hUT-A2 structure were shown (g) with the orientation distribution histogram figures (h) and the Fourier shell correlation curves (i) for the final 3D density map which was further colored according to local resolution (Å) (j). The cryo-EM density maps and models were shown for UTA_{inh}-F11 (k) and the main helices of UTA_{inh}-F11-hUT-A2 structure (l).

m-r. Calculation processes of the UTA_{inh}-A2-hUT-A2 structure using the cryoSPARC. Representative cryo-EM micrograph, 2D class averages and the refined map of UTA_{inh}-A2-hUT-A2 structure were shown (m) with the orientation distribution histogram figures (n) and the Fourier shell correlation curves (o) for the final 3D density map which was further colored according to local resolution (Å) (p). The cryo-EM density maps and models were shown for UTA_{inh}-A2 (q) and the main helices of UTA_{inh}-A2-hUT-A2 structure (r).

Supplemental Fig. 4

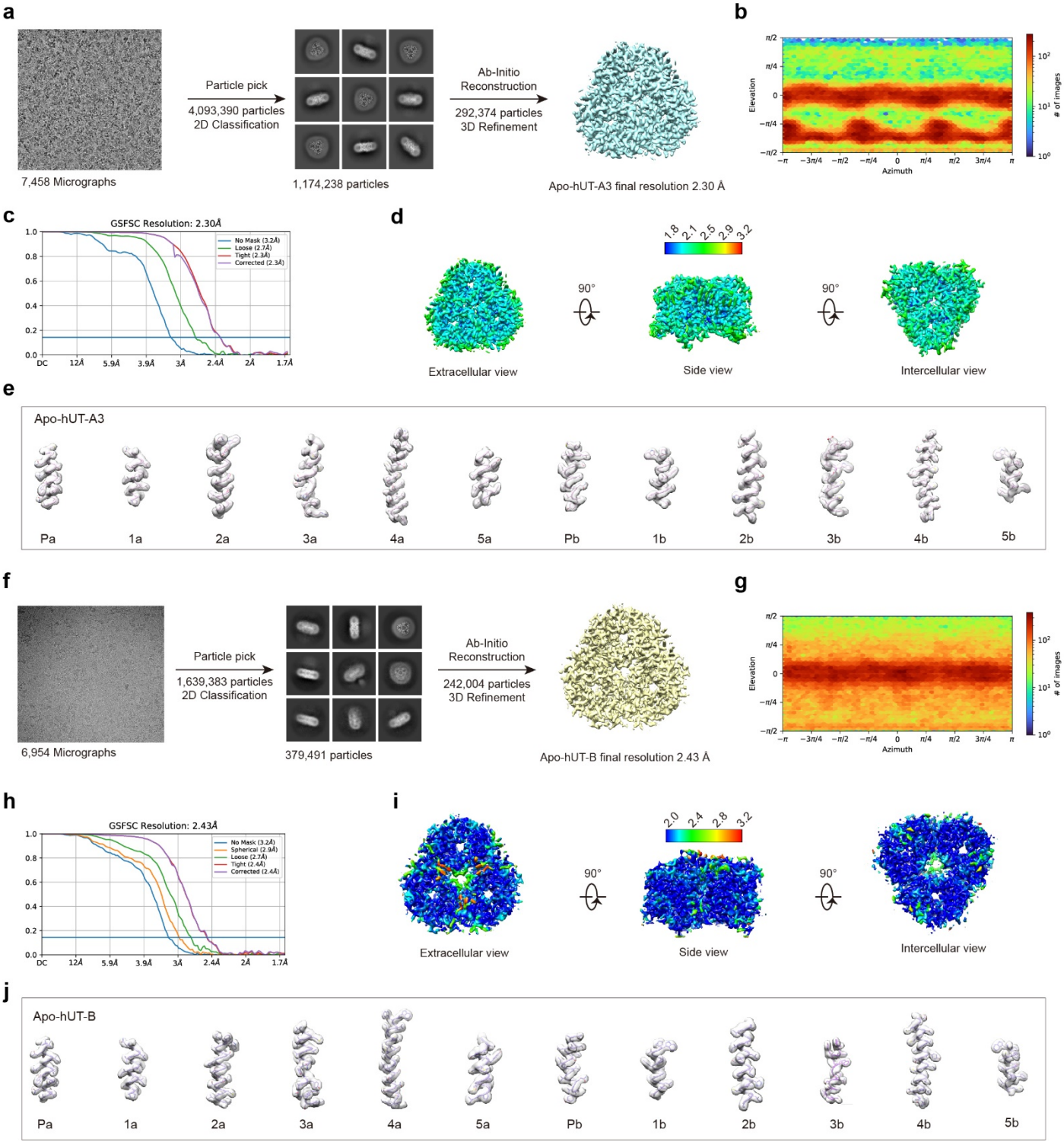

Supplementary Fig. 4 Processing of the calculation of the apo-hUT-A3 and apo-hUT-B structures.

a-e. Calculation processes of the apo-hUT-A3 structure using the cryoSPARC. Representative cryo-EM micrograph, 2D class averages and the refined map of apo-hUT-A3 structure were shown (a) with the orientation distribution histogram figures (b) and the Fourier shell correlation curves (c) for the final 3D density map which was further colored according to local resolution (d) (k). The cryo-EM density maps and models were shown for main helices of apo-hUT-A3 structure (e).

f-j. Calculation processes of the apo-hUT-B structure using the cryoSPARC. Representative cryo-EM micrograph, 2D

class averages and the refined map of apo-hUT-B structure were shown (f) with the orientation distribution histogram figures (g) and the Fourier shell correlation curves (h) for the final 3D density map which was further colored according to local resolution (Å) (i). The cryo-EM density maps and models were shown for main helices of apo-hUT-B structure (j).

Supplemental Fig. 5

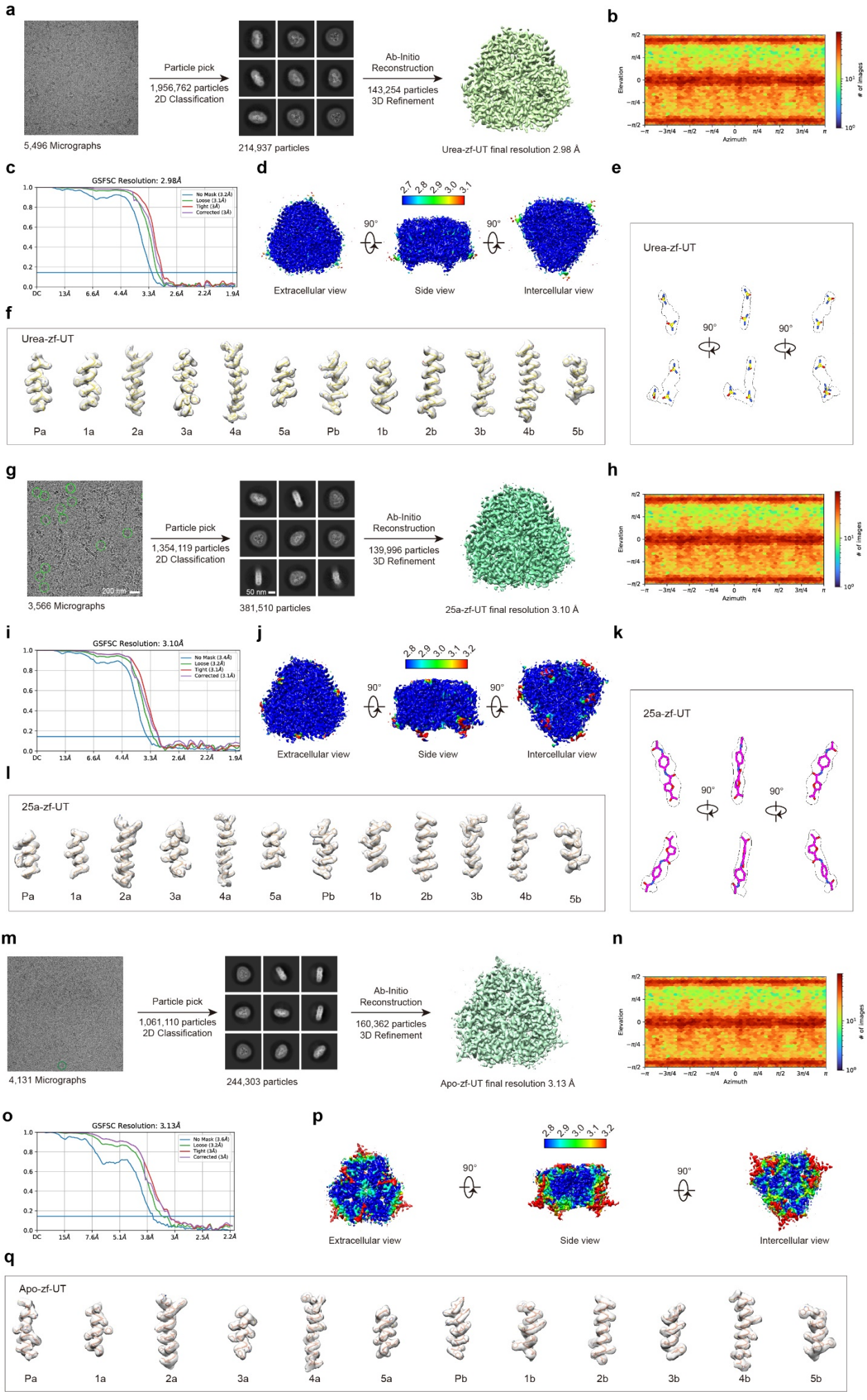

Supplementary Fig. 5 Calculation processes of the urea/25a/apo-zf-UT structures.

a-f. Calculation processes of the urea-zf-UT structure using the cryoSPARC. Representative cryo-EM micrograph, 2D class averages and the refined map of urea-zf-UT structure were shown (a) with the orientation distribution histogram figures (b) and the Fourier shell correlation curves (c) for the final 3D density map which was further colored according to local resolution (Å) (d). The cryo-EM density maps and models were shown for the urea (e) and main helices of urea-zf-UT structure (f).

g-l. Calculation processes of the 25a-zf-UT structure using the cryoSPARC. Representative cryo-EM micrograph, 2D class averages and the refined map of 25a-zf-UT structure were shown (g) with the orientation distribution histogram figures (h) and the Fourier shell correlation curves (i) for the final 3D density map which was further colored according to local resolution (Å) (j). The cryo-EM density maps and models were shown for 25a (k) and the main helices of 25a-zf-UT structure (l).

m-q. Calculation processes of the apo-zf-UT structure using the cryoSPARC. Representative cryo-EM micrograph, 2D class averages and the refined map of apo-zf-UT structure were shown (m) with the orientation distribution histogram figures (n and the Fourier shell correlation curves (o) for the final 3D density map which was further colored according to local resolution (Å) (p). The cryo-EM density maps and models were shown for the main helices of apo-zf-UT structure (q).

Supplemental Fig. 6

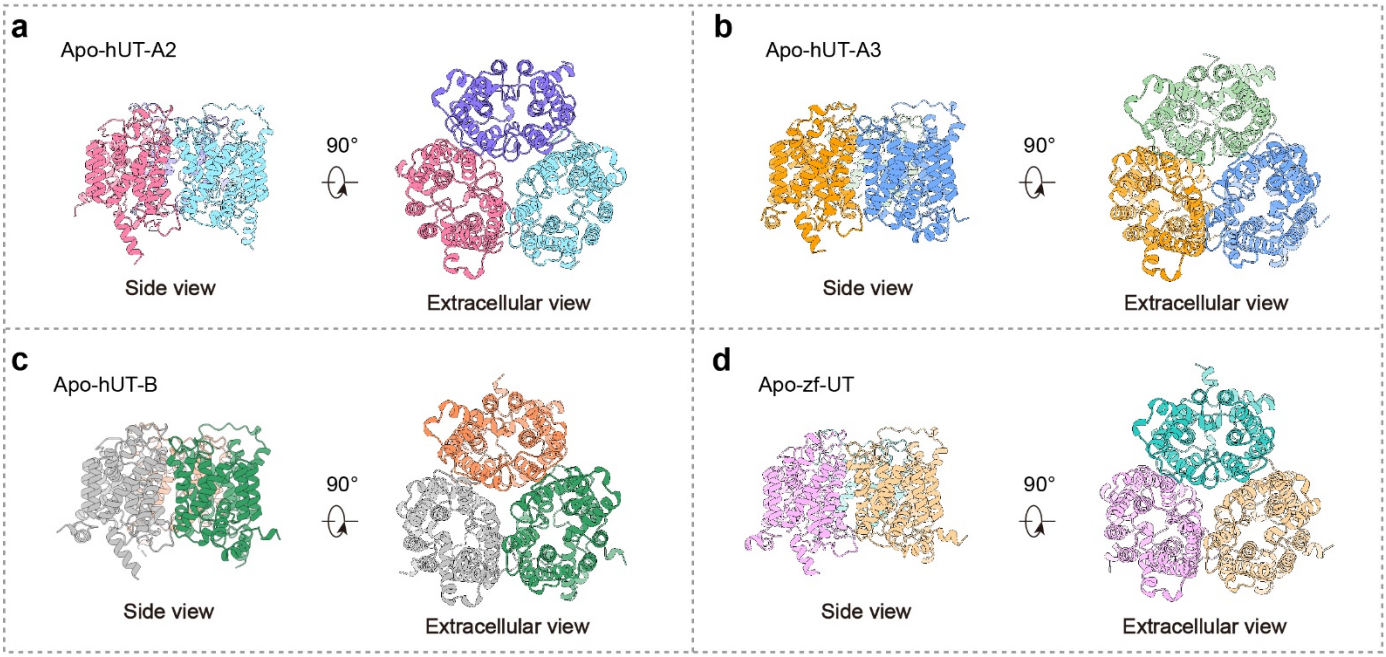

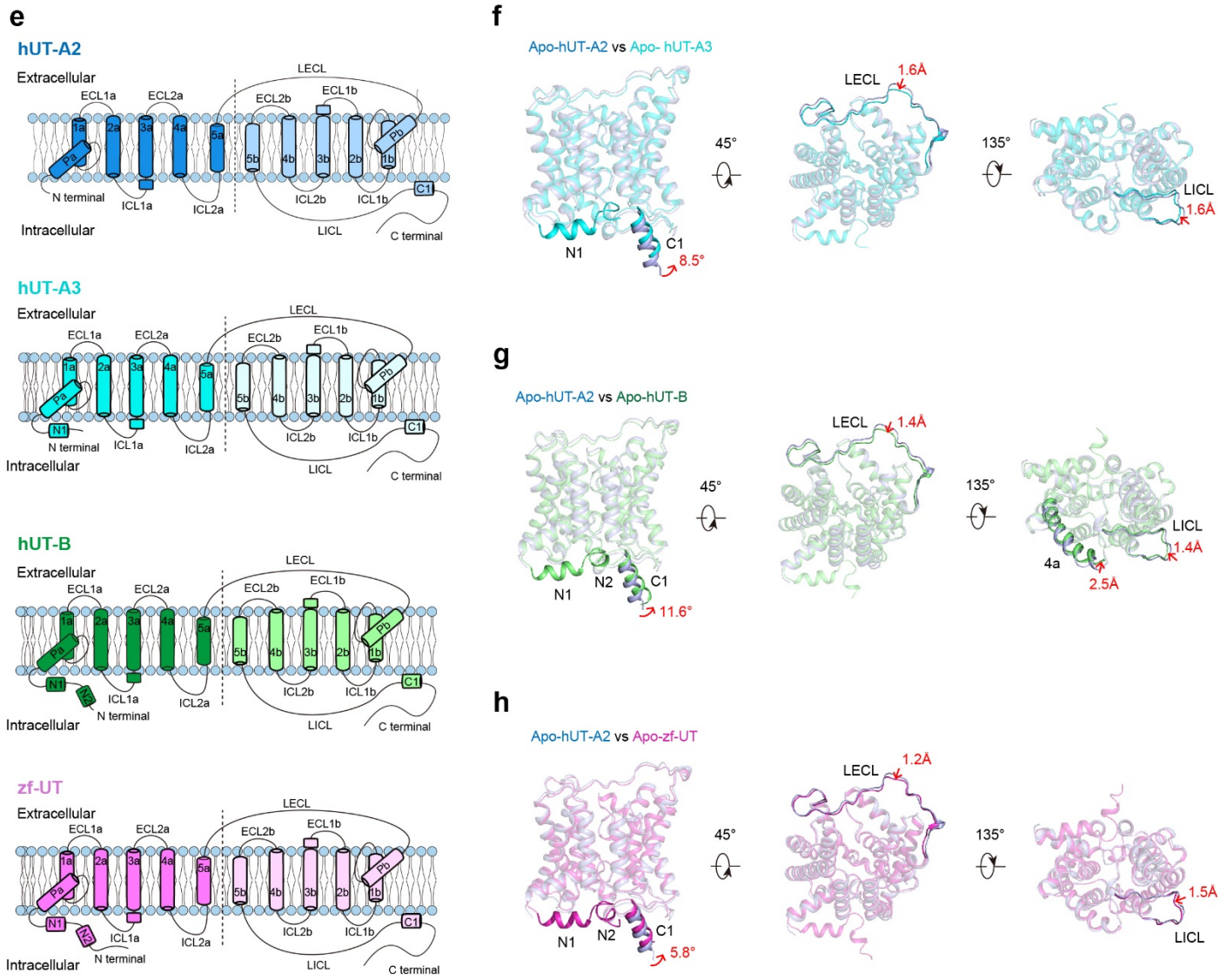

Supplementary Fig. 6 Structural representation and comparison between hUT-A2, hUT-A3, hUT-B and zf-UT.

a-d. Structural representations of apo-hUT-A2 homotrimer (a), apo-hUT-A3 homotrimer (b), apo-hUT-B homotrimer (c) and apo-zf-UT homotrimer (d), from the side view (left) and the extracellular view (right), respectively.

e. Diagram of the topology of transmembrane helices of hUT-A2, hUT-A3, hUT-B and zf-UT, oriented with the intracellular side on bottom, equivalent helices between the two homologous repeats are marked with a and b. ECL indicates the extracellular loop and the ICL indicates the intracellular loop. LECL (long extracellular loop). LICL (long intracellular loop).

f-h. Structural comparison between hUT-A2 and hUT-A3 (f), or hUT-B (g), or zf-UT (h).

Supplemental Fig. 7

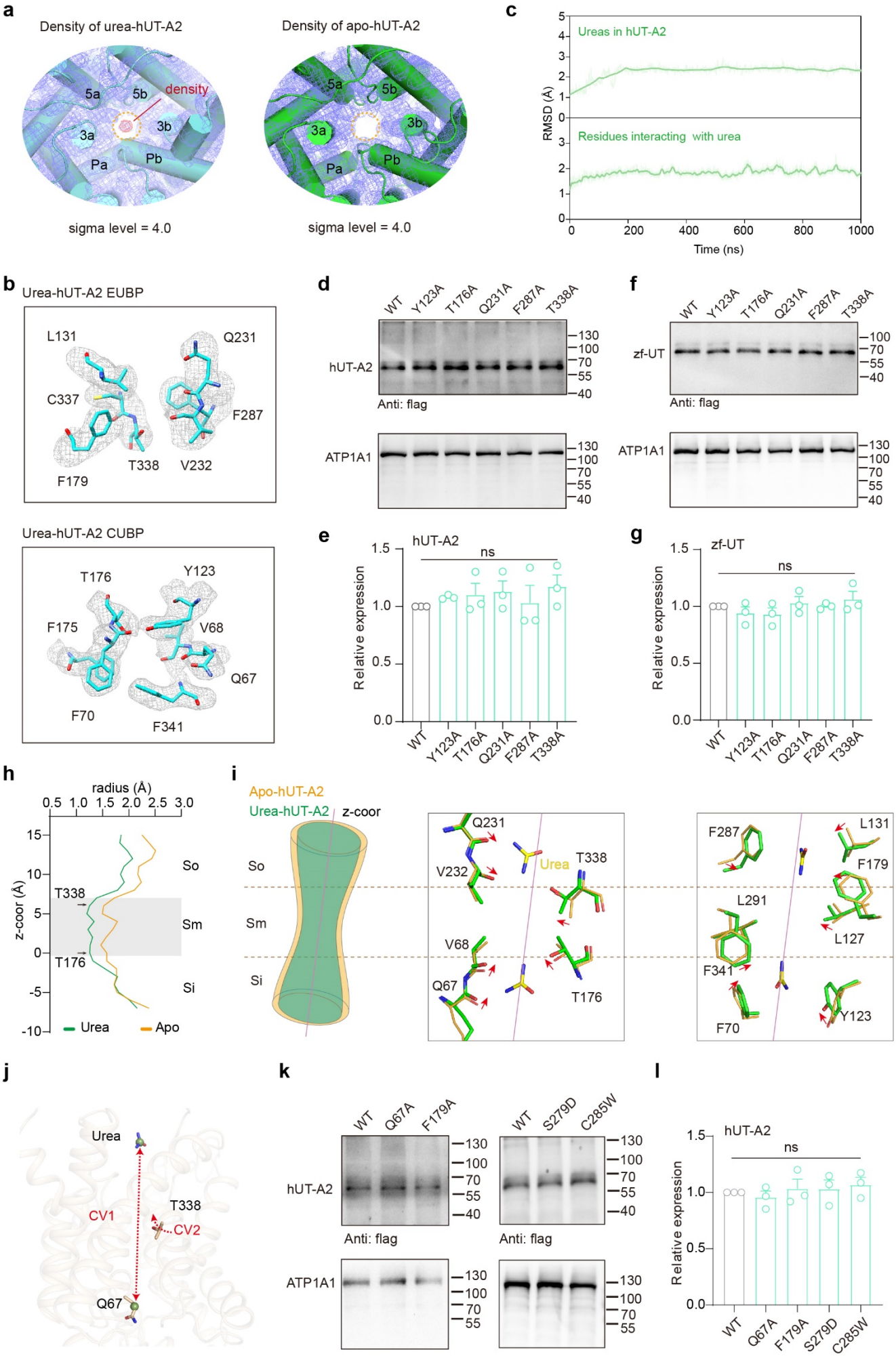

Supplementary Fig. 7 The urea transport mechanism of hUT-A2.

a. Comparison of the cryo-EM density (blue mesh) in the urea transport channel (orange dashed lines) of urea-hUT-A2 and apo-hUT-A2 structures. Unambiguous density (red mesh) was found in the urea-hUT-A2 but not the apo-hUT-A2 structures at the σ level of 4.0 in PyMOL.

b. The cryo-EM density (gray mesh) of the key residues of the EUBP and CUBP in the urea-hUT-A2 structures at the contour level of 1.300 V in UCSF Chimera.

c. RMSDs of the urea molecules (upper curve) and the residues interacting with urea (down curve) of urea-hUT-A2 in 1000 ns MD simulation.

d-e. Representative western images (d) and statistical analysis (e) of the expression of wild type hUT-A2 and its mutants were shown, using ATP1A1 for reference. Data are shown as mean ± SEM (n = 3). ns, no significant, compared with the wild type protein by unpair Student's t-test.

f-g. Representative western images (f) and statistical analysis (g) of the expression of wild type hUT-A2 and its mutants were shown, using ATP1A1 for reference. Data are shown as mean ± SEM (n = 3). ns, no significant, compared with the wild type protein by unpair Student's t-test.

h. Pore radii for urea-hUT-A2 (green line) and apo-hUT-A2 (orange line) calculated with the program Caver 3.0.3.

i. Comparison of the urea transport channel of urea-hUT-A2 (green) and apo-hUT-A2 (orange) structures. The channel were built according to the pore radii of these two structures (left panel), and the key residues with structural rearrangement were shown .

j. The collective variables in the MD simulations. The CV1 have set as the distance between the center of mass of urea and residue $Q67^{Pa}$, while CV2 has been modified to the dihedral angle of residue $T338^{5b}$ located in the upper half of the channel.

k-l. Representative western images (k) and statistical analysis (l) of the expression of wild type hUT-A2 and its mutants were shown, using ATP1A1 for reference. Data are shown as mean ± SEM (n = 3). ns, no significant, compared with the wild type protein by unpair Student's t-test.

Supplemental Fig. 8

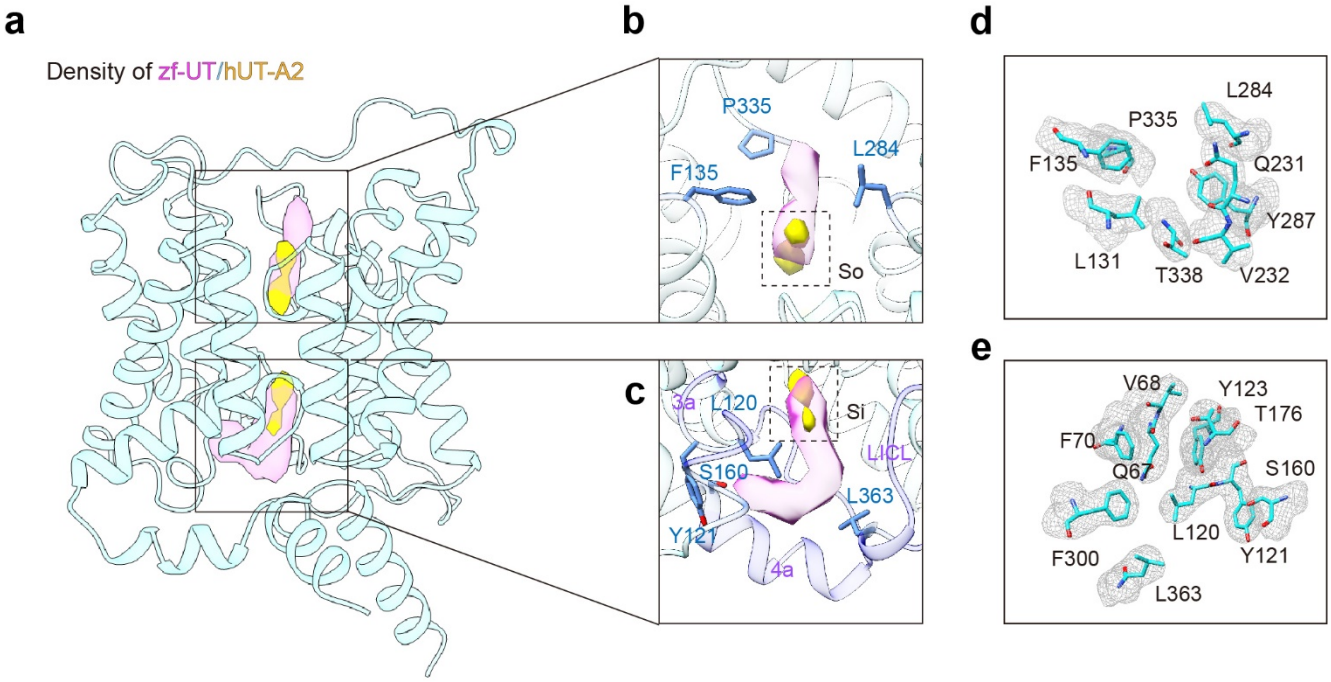

Supplementary Fig. 8 The urea transport mechanism of zf-UT.

a-c. Comparison of the cryo-EM density in the channel of apo-zf-UT (no density), urea-zf-UT (violet) and urea-hUT-A2 (yellow) structures. Compared with the apo-zf-UT and urea-hUT-A2 structures, obvious and continuous EM densities enabled easy assignment of urea on both the extracellular (b) and intracellular sides (c) of the zf-UT channel.

d-e. The cryo-EM density (gray mesh) of the key residues of the extracellular side (d) and intracellular side (e) of the channel of the urea-zf-UT structures at the contour level of 2.000 V in UCSF Chimera.

Supplemental Fig. 9

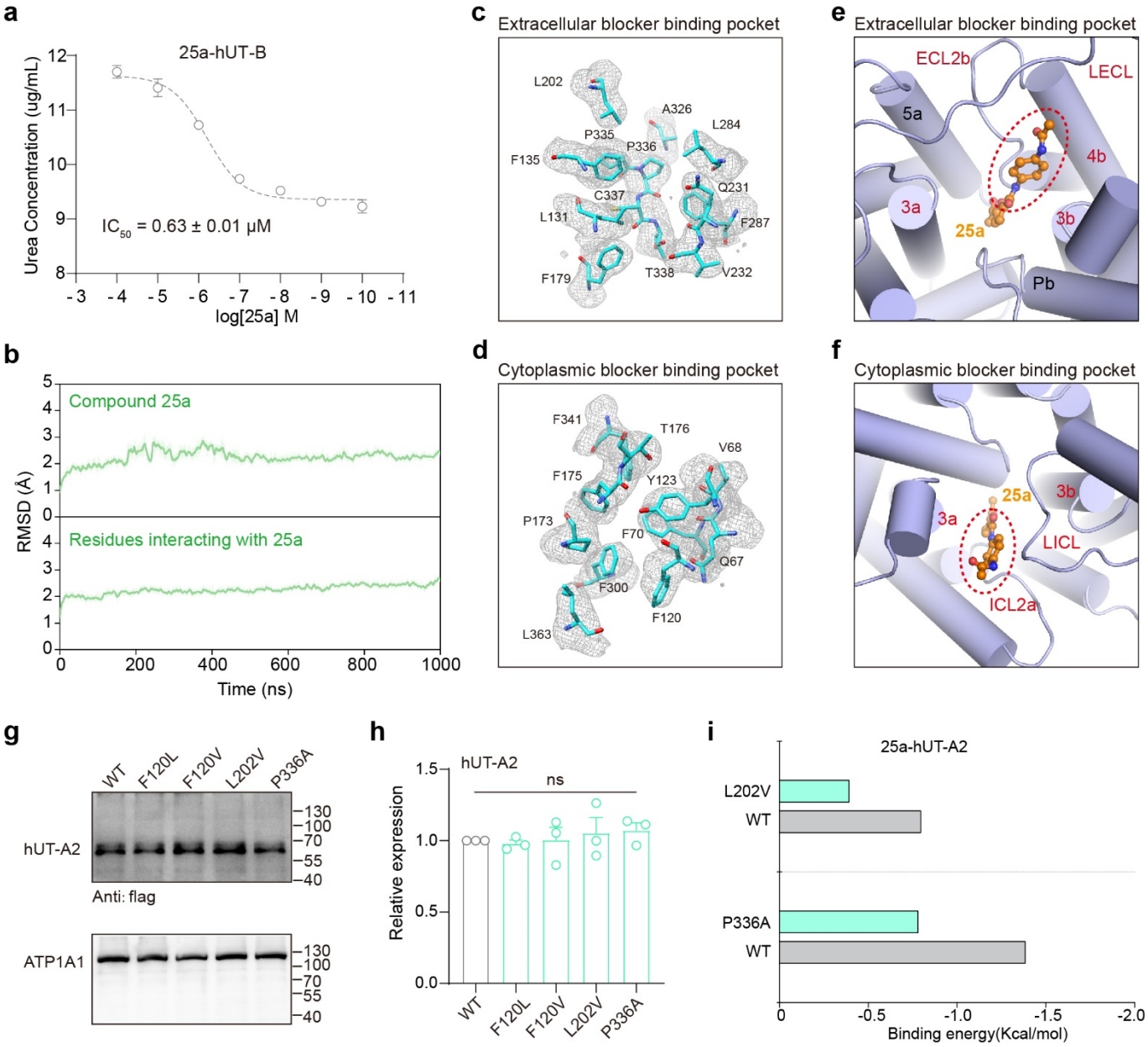

Supplementary Fig. 9 The mechanism of selective inhibition hUT-A2 by 25a.

a. The concentration dependent blockade of urea transport of hUT-B by 25a using urease assay. Data are shown as mean ± SEM of three independent experiments (n = 3).

b. Molecular dynamics simulation of the 25a-hUT-A2 structure. RMSDs of the 25a (upper curve) and the residues interacting with 25a (down curve) of 1000 ns MD simulation. The shaded area represents the original, unsmoothed value of distance, with reduced transparency, and the thick bold line was the result of smoothing averaging the original distance value every 200 points.

c-d. The cryo-EM density (gray mesh) of the key residues of the extracellular blocker binding pocket (EBBP) (c) and CUBP (d) of 25a in the 25a-hUT-A2 structures at the contour level of 0.100 V in UCSF Chimera.

e-f. The positions of EPPB1 (e) and EBBP2 (f) of 25a (orange stick-ball) in hUT-A2 structure were shown as circles by red dashed line. The helices and loops interacting with these two regions were marked red.

g-h. Representative western images (g) and the statistical analysis (h) showing the expression of wild type hUT-A2 and

its mutants in HEK293 transfected with the adjusted amount of plasmid, using the expression of ATP1A1 for reference. Data are shown as mean ± SEM of three independent experiments (n = 3). ns, no significant, compared with the expression of wild type protein by unpair Student's t-test (n = 3).

i. The comparison between best estimate residue energy contributions of residues L202 or P336 of wild type hUT-A2 for their interaction with 25a and best estimate residue energy contributions of their corresponding L202V, P336A mutants.

Supplemental Fig. 10

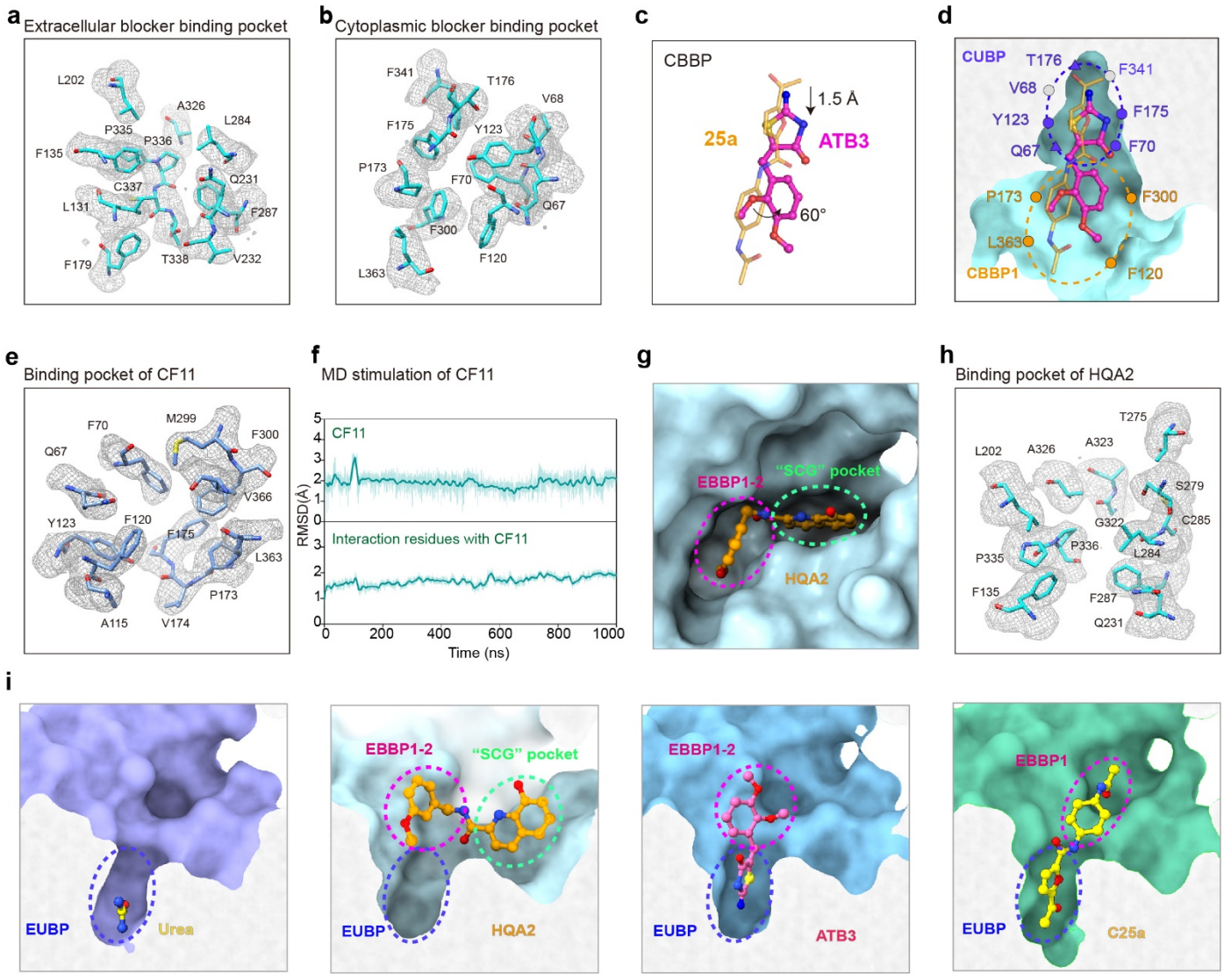

Supplementary Fig. 10 Mechanism of selective inhibition of hUT-A2 by inhibitors of ATB3, CF11 or HQA2.

a-b. The cryo-EM density (gray mesh) of the key residues of the extracellular blocker binding pocket (EBBP) (a) and CUBP (b) of ATB3 in the ATB3-hUT-A2 structure at the contour level of 0.100 V in UCSF Chimera.

c. The comparison of 25a and ATB3 in CBBP. The 25a and ATB3 were respectively represented by orange stick and magenta stick-ball.

d. The cutaway view of the binding pockets of ATB3 in cytoplasmic side. ATB3 occupied two subpockets, the CBBP1

and CUBP, which were shown as orange and blue dashed lines, respectively. Residues forming polar interactions or hydrogen bonds with ATB3 are depicted using triangles. Residues only forming hydrophobic or van der Waals interactions are depicted as solid round circles. The 25a and ATB3 were respectively represented by orange stick and magenta stick-ball. The hUT-A2 is represented by surface.

e. The cryo-EM density (gray mesh) of the key residues of the binding pocket of UTA_{inh}-F11 in the UTA_{inh}-F11-hUT-A2 structure at the contour level of 0.200 V in UCSF Chimera.

f. RMSD of CF11(upper panel) and the interacting residues with CF11 (lower panel) in CF11-hUTA2 during 1000 ns MD simulation. The shaded area represents the original, unsmoothed value of distance, with reduced transparency, and the thick line was the result of smoothing the original distance value every 200 points.

g. The top view of the HQA2 binding pocket of HQA2-hUT-A2 structure. The HQA2 was shown as orange stick-ball and the hUT-A2 was displayed as light cyan surface. The SCG pocket and EBBP1-2 were shown as green and violet dashed lines, respectively.

h. The cryo-EM density (gray mesh) of the key residues of the binding pocket of HQA2 in the HQA2-hUT-A2 structure at the contour level of 0.080 V in UCSF Chimera.

i. The comparison of the cutaway view of the binding pocket of urea, HQA2, ATB3 and 25a in the extracellular side of hUT-A2.

Supplementary table 1. Data collection and refinement statistics

	Apo-hUT-A2	Urea-hUT-A2	25a-hUT-A2	ATB3-hUT-A2	CF11-hUT-A2	HQA2-hUT-A2
Magnification	130,000	130,000	130,000	130,000	130,000	130,000
Voltage (kV)	300	300	300	300	300	300
Electron exposure (e^{-}/Å^2)	60	60	60	60	60	60
Defocus range (μm)	-0.8 ~ -2.0	-0.8 ~ -2.0	-0.8 ~ -2.0	-0.8 ~ -2.0	-0.8 ~ -2.0	-0.8 ~ -2.0
Pixel size (Å)	0.85	0.92	0.82	0.82	0.82	0.82
Symmetry imposed	C3	C3	C3	C3	C3	C3
Initial particle images (no.)	1,956,762	135,411,9	4,093,390	1,132,559	1,430,030	2,458,801
Final particle images (no.)	143,254	139,996	292,374	102,413	93,021	92,767
Map resolution (Å)	2.8	3.0	2.6	3.3	3.0	3.0
FSC threshold	0.143	0.143	0.143	0.143	0.143	0.143
Map resolution range (Å)	2.0 ~8.5	2.1 ~8.0	2.0 ~8.0	2.2 ~9.0	2.2 ~8.5	2.2 ~8.5
Initial model used (PDB code)	3K3F	3K3F	3K3F	3K3F	3K3F	3K3F
Model composition						
Non-hydrogen atoms	9599	7620	7599	7635	7656	7665
Protein residues	993	984	984	993	993	993
Ligands	0	6	6	6	3	3
B factors (Å^2)						
Protein	3	3	3	3	3	3
Ligand	0	6	6	6	3	3
R.m.s. deviations						
Bond lengths(A)	0.005	0.008	009	0.008	0.006	0.005
Bond angles (°)	1.099	1.162	1.317	1.220	1.174	0.649
Validation						
MolProbity score	1.65	1.73	1.74	1.91	1.65	1.71
Clash score	9.02	10.08	12.06	10.13	7.96	11.32
Ramachandran Plot						
Favored	97.26	96.93	97.24	95.44	96.66	97.26
Allowed	2.74	3.07	2.76	4.56	3.34	2.74
Disallowed	0	0	0	0	0	0

Supplementary table 2. Data collection and refinement statistics

	Apo-hUT-A3	Apo-hUT-B	Apo-zf-UT	Urea-zf-UT	25a-zf-UT
Magnification	130,000	130,000	130,000	130,000	130,000
Voltage (kV)	300	300	300	300	300
Electron exposure (e^{-}/Å^2)	60	60	60	60	60
Defocus range (μm)	-0.8 ~ -2.0	-0.8 ~ -2.0	-0.8 ~ -2.0	-0.8 ~ -2.0	-0.8 ~ -2.0
Pixel size (Å)	0.82	0.82	1.055	0.92	0.92
Symmetry imposed	C3	C3	C3	C3	C3
Initial particle images (no.)	4,093,390	1,639,383	1,061,110	1,956,762	1,354,119
Final particle images (no.)	292,374	242,004	160,362	143,254	139,996
Map resolution (Å)	2.3	2.4	3.1	3.0	3.1
FSC threshold	0.143	0.143	0.143	0.143	0.143
Map resolution range (Å)	1.8 ~6.0	1.9 ~6.0	2.6~7.0	2.5~7.0	2.6~7.5
Initial model used (PDB code)	3K3F	3K3F	3K3F	3K3F	3K3F
Model composition					
Non-hydrogen atoms	8013	8031	7938	8130	8262
Protein residues	1035	1050	1050	1074	1074
Ligands	0	0	0	15	3
B factors (Å^2)					
Protein	3	3	3	3	3
Ligand	0	0	0	15	6
R.m.s. deviations					
Bond lengths(A)	0.005	0.005	0.010	0.009	0.011
Bond angles (°)	0.531	0.562	1.232	1.175	1.351
Validation					
MolProbity score	1.52	1.46	1.67	1.82	1.76
Clash score	6.25	6.34	10.11	11.45	12.70
Ramachandran Plot					
Favored	96.99	97.41	97.22	96.35	97.19
Allowed	3.01	2.59	2.78	3.65	2.81
Disallowed	0	0	0	0	0

Supplementary table 3. Information of the cryo-EM map and the structures

Structures	Model	Map	Contour level	Residues number
Apo-hUT-A2	hUTA2-Apo-n-coot-2	hUTA2-Apo-n-Zmap	4.80 rmsd	K51-R381
Urea-hUT-A2	hUTA2-Urea-coot-33	hUTA2-Urea-mapZS	5.50 rmsd	S52-Q379
25a-hUT-A2	hUTA2-25a-coot-25	hUTA2-25a-mapS	4.30 rmsd	S52-Q379
ATB3-hUT-A2	hUTA2-B3-coot-31	hUTA2-B3-map	3.80 rmsd	K51-R381
CF11-hUT-A2	hUTA2-F11-coot-30	hUTA2-F11-map	3.00 rmsd	K51-R381
HQA2-hUT-A2	hUTA2-A2-coot-20	hUTA2-A2-mapS	4.00 rmsd	K51-R381
Apo-hUT-A3	hUTA3-Apo-coot-2	hUTA3-Apo-J100-mapS	4.50 rmsd	G96-V440
Apo-hUT-B	hUT-B-Apo-coot-8	hUTB-Apo-ZSmap	4.80 rmsd	A34-R383
Apo-zf-UT	ZFUT-Apo-coot-4	ZFUT-Apo-mapS	7.00 rmsd	I31-K380
Urea-zf-UT	ZFUT-Urea-coot-25	ZFUT-Urea-Zmap	6.00 rmsd	A28-T385
25a-zf-UT	ZFUT-25a-coot-32	ZFUT-25a-map	4.30 rmsd	K27-K381

Supplementary table 4. The IC_{50} and inhibition modes of the different UT inhibitors.

Inhibitor	IC50 (μM)			inhibition mode	Reference
	UT-A2	UT-A1	UT-B		
25a	0.58 ± 0.01	< 8.0	0.63 ± 0.01	competitive	*Eur J Med Chem. 226:113859*
ATB3	6.38 ± 0.54	~ 7.0	~ 43	competitive	*Chem Biol. 20(10):1235-44*
CF11	2.78 ± 0.32	~ 1.0	~ 10.0	un-competitive	*FASEB J. 28(9):3878-90*
HQA2	3.66 ± 0.09	~ 5.3	> 50	non-competitive	*Chem Biol. 20(10):1235-44*

Supplementary table 5. The interaction betweens 25a and hUT-A2

Residues	Interaction	Distance (Å)
Extracellular blocker binding pocket		
L131	Hydrophobic or van der Waals forces≤4.0 Å	3.3
F135		3.9
F179		4.0
L202		3.7
Q231	Polar interaction ≤4.0 Å	3.9
V232	Hydrophobic or van der Waals forces≤4.0 Å	2.9
L284		3.8
F287		3.5
A326		4.0
P335		3.6
P336		3.6
C337		3.6
T338	H-Bond ≤3.5 Å	2.5
Cytoplasmic blocker binding pocket		
Q67	Polar interaction ≤4.0 Å	3.9
V68	Hydrophobic or van der Waals forces≤4.0 Å	3.2
F70		3.0
F120		3.3
Y123		3.3
P173		3.8
F175		3.3
T176	H-Bond ≤3.5 Å	3.1
F300	π-π stacking ≤6.0 Å	4.5
F341	Hydrophobic or van der Waals forces≤4.0 Å	3.6
L363		3.8

Supplementary table 6. The interactions between ATB3 and hUT-A2

Residues	**Interaction**	**Distance (Å)**
Extracellular blocker binding pocket		
L131	Hydrophobic or van der Waals forces≤4.0 Å	3.9
F135	π-π stacking ≤6.0 Å	3.3
L202	Hydrophobic or van der Waals forces≤4.0 Å	3.5
Q231	H-bond ≤3.5 Å	3.0/3.3
V323	Polar interaction ≤4.0 Å	3.8
F282	π-π stacking ≤6.0 Å	4.7
L284	Hydrophobic or van der Waals forces≤4.0 Å	3.3
F287		3.5
P336		3.5
C337		4.0
T338	H-Bond ≤3.5 Å	3.2

Cytoplasmic blocker binding pocket		
Q67	H-Bond ⩽3.5 Å	3.2
F70	Hydrophobic or van der Waals forces⩽4.0 Å	3.6
F120		3.3
Y123	Polar interaction ⩽4.0 Å	3.6
P173	Hydrophobic or van der Waals forces⩽4.0 Å	3.8
F175		3.8
T176	Polar interaction ⩽4.0 Å	4.0
F300	Hydrophobic or van der Waals forces⩽4.0 Å	4.0
L363		3.4

Supplementary table 7. The interactions between CF11 and hUT-A2

Residues	**Interaction**	**Distance (Å)**
Q67	Hydrophobic or van der Waals forces⩽4.0 Å	3.7
F70		3.5
A115		3.2
F120	π-π stacking ⩽6.0 Å	3.8
Y123	Polar interaction ⩽4.0 Å	3.6
P173	Hydrophobic or van der Waals forces⩽4.0 Å	3.2
V174	H-Bond ⩽3.5 Å	3.4
F175	Polar interaction ⩽4.0 Å	3.8
M299	Hydrophobic or van der Waals forces⩽4.0 Å	4.0
F300	π-π stacking ⩽6.0 Å	3.9
L363	Hydrophobic or van der Waals forces⩽4.0 Å	3.8
V366		3.0

Supplementary table 8. The interactions between HQA2 and hUT-A2

Residues	**Interaction**	**Distance (Å)**
F135	π-π stacking ⩽6.0 Å	3.6
L202	Hydrophobic or van der Waals forces⩽4.0 Å	3.6
Q231	H-bond ⩽3.5 Å	3.2
T275	Hydrophobic or van der Waals forces⩽4.0 Å	4.0
S279	H-bond ⩽3.5 Å	3.4
F282	Hydrophobic or van der Waals forces⩽4.0 Å	3.6
L284		3.3
C285		3.5
F287		3.9
G322		3.9
A323		3.9
A326		3.7
P335		3.6
P336		3.2

Supplementary table 9. The statistic of the free energy in MD stimulation on different UTs.

Structural models	Valley values of the free energy ΔG(kcal/mol)			Energy barriers ΔΔG(kcal/mol)		Reference
	So	Sm	Si	So-Sm	Si-Sm	
hUT-A2-Urea	-3.4	0	-2.7	8.0	6.6	This paper
zf-UT-Urea	-4.4	0	-3.3	9.8	7.6	This paper
hUT-B (PDB: 6QD5)	-2.4	3.0	-2.5	6.0	6.5	*Molecular Simulation, 47(12), 1022–1028.*
Bos-UT-B (PDB: 4EZC)	0	3.0	0	4.0	4.8	*Proc Natl Acad Sci U S A 109: 11194-11199*
*Hp*UreI (PDB: 3UX4)	0	1.3	0.3	2.1	3.1	*Nat Commun. 2013;4:2900.*

Supplementary table 10. Membrane Permeability Prediction of CF11 (UTA_{inh}-F11).

Membrane Permeability Prediction of CF11 (UTA_{inh}-F11)			
[1]Log Perm RRCK (cm/s)	[2]Membrane HDLD	[3]Membrane GB	[4]Membrane *dG Insert
-4.963	10.851	−8.788	11.020

[1]Log Perm RRCK: logarithm of the RRCK permeability in cm/s. This property is optimized to reproduce RRCK permeability assay results, with fitted energy; [2]Membrane HDLD: the free energy penalty for the neutral form of the ligand in its conformation inside the membrane to enter the membrane (i.e., move from the high dielectric region to the low dielectric region, hence HDLD). [3]Membrane GB: an implicit membrane generalized born theory model closely reproduces the Poisson–Boltzmann (PB) electrostatic solvation energy profile across the membrane. [4]*Partition energy "dG" Insert prediction; Membrane dG Insert: the total free energy penalty for the ligand to change state and enter the membrane. This is the net of the energy of Membrane HDLD and Membrane State Penalty.